



# Critical behavior of the order-disorder phase transition in $\beta$ -brass investigated by x-ray scattering

A. Madsen,<sup>1,\*</sup> J. Als-Nielsen,<sup>2</sup> J. Hallmann,<sup>1</sup> T. Roth,<sup>1</sup> and W. Lu<sup>1</sup>

<sup>1</sup>European X-Ray Free-Electron Laser Facility, Holzkoppel 4, D-22869 Schenefeld, Germany

<sup>2</sup>Niels Bohr Institute, University of Copenhagen, Universitetsparken 5, DK-2100 Copenhagen Ø, Denmark

(Received 19 May 2016; published 13 July 2016)

$\beta$ -brass exhibits an archetypical example of an order-disorder transition with a critical behavior that was previously investigated by neutron scattering. The data were well described by the three-dimensional (3d) Ising model but the relatively crude experimental resolution prevented an in-depth examination of the single-length scaling hypothesis, a cornerstone in the theory of critical phenomena. With the development of synchrotron x-ray experiments, high-resolution data could be recorded and surprisingly it was found that the single-length scaling did not hold in most critical systems, possibly due to strain originating from surface defects and/or impurities. In this paper we demonstrate single-length critical behavior using high-resolution x-ray scattering in  $\beta$ -brass. The investigations confirm that  $\beta$ -brass behaves like a 3d Ising system over a wide range of length scales comprising correlated clusters of millions of atoms. To vary the surface sensitivity, experiments have been performed both in Bragg reflection and Laue transmission geometries but without any substantial differences observed in the scaling and critical behavior.

DOI: 10.1103/PhysRevB.94.014111

## I. INTRODUCTION

$\beta$ -brass is a 1:1 alloy of Cu and Zn that provides an archetypical example of a continuous order-disorder phase transition [1] with a critical behavior that is well described by the Ising model [2]. Above a critical temperature  $T_C = 739$  K the occupation of lattice sites is random with equal probabilities to find Cu and Zn atoms at a given site in the body-centered cubic (bcc) lattice which can be thought of as two simple cubic lattices displaced half a cube diagonal relative to each other (lattice constant  $a \approx 2.95$  Å). Below  $T_C$ , long-range order (LRO) develops with Cu atoms predominantly on one of the cubic lattices and Zn atoms predominantly on the other one, as described quantitatively by an order parameter  $S_r$  being +1 (−1) for right (wrong) occupation of site  $\mathbf{r}$  in any of the two lattices. The average value of  $S_r$ , here denoted  $\langle S \rangle$ , is close to unity at room temperature but vanishes at the critical temperature as a power law  $\langle S \rangle \propto (T_C - T)^\beta$ . The angular brackets  $\langle \cdot \rangle$  denote a thermal average, i.e., averaging over a large volume and/or over times much longer than a typical time scale for occupational changes of (many) lattice sites. This averaging is fulfilled in the experiments presented here.

In an x-ray or neutron scattering experiment the diffraction pattern from a bcc lattice displays reflections at Miller indices  $(h00)$ ,  $h$  being an even integer. The Bragg angle for the reflection is  $\theta_B = \sin^{-1}(\frac{\lambda h}{2a})$ , where  $\lambda$  is the x-ray wavelength. In addition, below  $T_C$  in  $\beta$ -brass superlattice reflections emerge at  $(h00)$ , where  $h$  is an odd integer. The superlattice structure factor is proportional to  $\langle S \rangle$  times  $(f_{\text{Zn}} - f_{\text{Cu}})$ , the difference between the scattering lengths (atomic form factors) of Zn and Cu, and the intensity is proportional to the absolute square of the structure factor.

Although the order parameter  $\langle S \rangle$  vanishes at  $T_C$ , a finite average correlation (SRO, short-range order) between the order parameter at site 0 and site  $\mathbf{r}$  still persists above  $T_C$ , approximately given by the Ornstein-Zernike correlation

function  $\langle S_0 S_r \rangle = e^{-\kappa r}/r$ , where  $\kappa^{-1}$  is a correlation length. The concomitant scattering, so-called critical scattering, is the three-dimensional (3d) Fourier transform of  $\langle S_0 S_r \rangle$  and hence has a Lorentzian line shape  $\chi(q) \propto 1/(q^2 + \kappa^2)$ , where  $q$  is the modular difference between the incoming and outgoing scattering vectors  $\mathbf{k}$  and  $\mathbf{k}'$  and the reciprocal lattice vector  $\mathbf{G}_h$ , i.e.,  $q = |\mathbf{k} - \mathbf{k}' - \mathbf{G}_h|$ .

The scattering thus depends both on  $q$  and the relative temperature difference from  $T_C$  as illustrated in Fig. 1(a). The LRO is determined by the superlattice Bragg intensity, confined to the  $q = 0$  half plane with  $T < T_C$  (turquoise). The critical scattering (red curve) is maximal at  $q = 0$  where it diverges as the power law  $C_\pm \times |1 - T/T_C|^{-\gamma}$ , the subscript  $\pm$  indicating temperatures above and below  $T_C$ . The ratio  $C_+/C_-$  is theoretically around 5.2 [3] as indicated by the asymmetry of the full and dotted red lines in the  $q = 0$  plane. The correlation length relative to the nearest-neighbor distance,  $\kappa^{-1}/a_{nn}$ , diverges at the critical temperature as a power law  $|1 - T_C/T|^{-\nu}$ , where  $a_{nn} = a\sqrt{3}/2$  is the distance between nearest-neighbor atoms. Figure 1(b) illustrates reciprocal space in the  $(h, k, l = 0)$  plane with red spots indicating fundamental reflections ( $h + k$  even) and superlattice reflections ( $h + k$  odd) shown by blurred circles.

The theoretical predictions of the critical exponents for the 3-dimensional Ising model are  $\beta = 0.313$ ,  $\gamma = 1.25$ , and  $\nu = 0.643$  [3,4]. These predictions hold for an infinite bulk sample, so eventual surface effects are not considered. The order-disorder transition in  $\beta$ -brass has previously been studied in great detail by neutron scattering [5–7] on large samples (volume of order 1 cm<sup>3</sup>), so in these studies surface effects could safely be neglected. For an x-ray energy of 12 keV the  $1/e$  absorption length in Cu-Zn is  $\sim 7$   $\mu\text{m}$  and surface effects may indeed be of importance in reflection geometry with a penetration depth of only  $7 \mu\text{m} \times \frac{\sin \theta_B}{2} \simeq 0.6 \mu\text{m}$  at the (100) reflection.

The angular divergence of a neutron beam is typically larger than about 0.2° which is two orders of magnitude higher than for synchrotron x-ray beams, resulting in a comparatively crude resolution in  $q$  space, so that correlation lengths longer

\*anders.madsen@xfel.eu

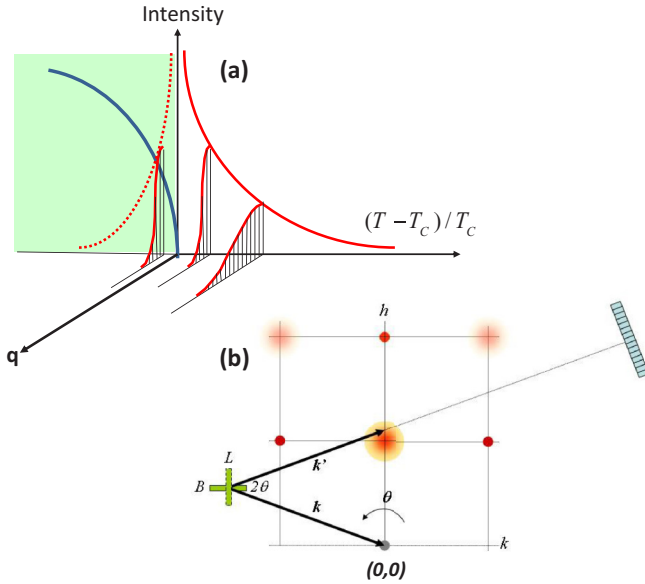


FIG. 1. (a) Sketch of the scattering from  $\beta$ -brass where the blue curve indicates Bragg scattering (LRO) and the red curves critical scattering (SRO). (b) Reciprocal  $(h, k)$  plane showing the fundamental reflections as red dots and superlattice reflections as blurred circles. The sample crystal is shown both in symmetric Laue (L) and symmetric Bragg reflection (B) orientations. The linear or area detector, shown in blue, has pixels as indicated.

than  $\sim 20 a_{nn}$  could not be determined in those earlier studies. Another contribution to the  $q$  resolution comes from the mosaicity of the single-crystal sample. As discussed in the next section, annealing of the  $\beta$ -brass crystals resulted in a mosaic width of less than  $0.01^\circ$  so in principle much longer correlation ranges than have been determined by neutron scattering [8] should become accessible in this experiment. A further limit may be set by the temperature stability but if, relative to  $T_C$ , it is  $\sim 10^{-4}$  or better, correlation lengths larger than  $\sim 200 a_{nn}$  are within reach.

$\beta$ -brass was not studied extensively with x-ray scattering earlier due to the pertinent problem of dezincification close to  $T_C$  that we address in the next section. However, other critical systems of both first and second order have been investigated with high-resolution x-ray scattering, always resulting in the observation of a second critical length scale much larger than the one predicted by the Ising model. It has been suggested that surface defects and associated strain play a role and that the phenomenon originates from a skin layer with several tens of microns thickness; see Cowley's review article [9] for additional information. Despite great efforts being devoted to perfecting the sample preparation, neither critical systems exhibiting displacive structural phase transformations or magnetic transitions have yielded the expected single-length scaling. In this paper we unambiguously show that the order-disorder transition in  $\beta$ -brass indeed is exhibiting single-length critical behavior over a substantial length scale comprising correlated clusters of millions of atoms in comparison with the limit of thousands of atoms from the previous neutron scattering experiments.

The paper is organized as follows: In Sec. II the sample preparation and initial crystal characterization are described; the results of critical scattering experiments in Laue and Bragg geometries are presented in Secs. III and IV, respectively. Finally, Sec. V summarizes the results of LRO and SRO investigations in the two different scattering geometries and the findings are discussed in relation with the aforementioned critical x-ray scattering results obtained in different systems. The Appendix contains a detailed discussion of dynamical scattering theory in Laue geometry.

## II. SAMPLE PREPARATION AND INITIAL CHARACTERIZATION

Beta brass crystal boules grown by the Bridgman-Stockbarger technique were purchased from Metal Crystals and Oxides Ltd. (UK) and MaTeck GmbH (Germany). Square-shaped platelets ( $3.5 \times 3.5 \text{ mm}^2$ ) with  $\langle 100 \rangle$  normal and a thickness of about  $50\text{--}100 \mu\text{m}$  were cut and polished from the boule. In order to avoid loss of Zn at elevated temperatures, the crystals must be encapsulated. This was obtained by positioning the crystals in  $330 \mu\text{m}$  deep indentations, etched into a  $\langle 100 \rangle$  standard Si wafer of  $350 \mu\text{m}$  thickness, leaving a Si single crystalline membrane approximately  $20 \mu\text{m}$  thick over the  $\beta$ -brass crystal. Subsequently, the wafer was bonded hermetically to a  $0.5 \text{ mm}$  Pyrex glass plate by applying  $500\text{--}1000$  volts across the glass/Si interface at  $\sim 620 \text{ K}$  for about two hours. The bonded Pyrex-Si wafer was then cut up into  $7 \times 7 \text{ mm}^2$  squares around each  $\beta$ -brass crystal. The encapsulated crystal is sketched in Fig. 2, both in Bragg reflection and Laue transmission geometry. The crystal is under vacuum in the cavity and was neither fixed to the Si crystal nor to the Pyrex glass, but the slanted faces of the Si indentation and a tight fit prevented it from rattling. The encapsulation procedure explained above was carried out by DTU Danchip (Denmark).

The encapsulated sample was kept in a custom-made vacuum furnace during the measurements to control the temperature. Beam access to the sample was either provided by transparent windows (Kapton) or by directly connecting the furnace to the beamline's vacuum tube. The sample holder and environment were made of Cu, and a resistive heater connected to a Lakeshore PID temperature controller with feedback from a Pt-100 sensor ensured good stability. Several sensors were mounted in the sample holder Cu block but there was no Pt-100 directly on the sample due to its encapsulation. The furnace was installed on the spectrometer's sample table where a high-precision goniometer provided access to the necessary motions.

As explained above, during the encapsulation process the samples were heated to about  $620 \text{ K}$  for approximately 2 hours. Before annealing the samples were mosaic crystals with a FWHM of the  $(100)$  rocking curves of about  $1.4^\circ$ . After annealing the crystal has become nearly perfect with a few millidegrees wide rocking curve. This evolution is shown in Fig. 3. The width is reduced by almost 3 orders of magnitude and the data evidence a perfect crystal structure with a Darwin width  $\Delta\lambda/\lambda = \Delta\theta/\tan\theta$  on the order of  $7.5 \times 10^{-4}$ . A Si(111) monochromator has been used for all measurements with an intrinsic resolution of  $1.4 \times 10^{-4}$ .

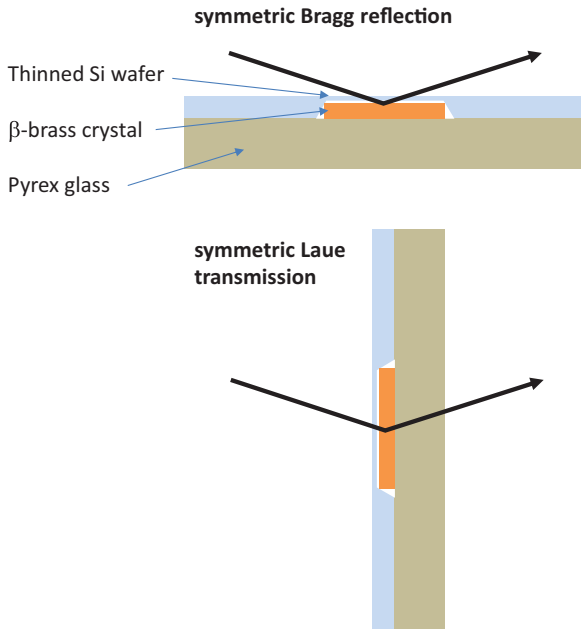


FIG. 2. Encapsulation of  $\beta$ -brass crystal. A Si wafer with an indentation fitting the  $\beta$ -brass crystal is bonded to a Pyrex glass plate providing a hermetically closed container. In the Laue case (21 or 25 keV x rays) the measured absorption of the beam traversing 20  $\mu\text{m}$  Si,  $\beta$ -brass, and 500  $\mu\text{m}$  Pyrex glass was used to calculate the thickness of the  $\beta$ -brass crystal, typically  $\sim 70 \mu\text{m}$ . In the Bragg case (12 keV x rays) absorption implies that only a  $\sim 0.6 \mu\text{m}$  thick near-surface layer is probed by the beam, i.e., less than 100 times the actual crystal thickness.

Hence, the width of the  $\beta$ -brass reflections can be found by deconvolution, and using a simple Gaussian approximation one obtains  $7.4 \times 10^{-4}$ . This is only a few times larger than for highly perfect Si single crystals and implies that at least the fundamental reflections should be analyzed in terms of dynamical diffraction theory. This abnormal growth of a single grain was observed for all the encapsulated crystals used in this study. A similar phenomenon has previously been reported by use of transmission electron microscopy in  $\beta$ -brass annealed at temperatures close to  $T_C$  [10].

We investigated the issue of dynamical diffraction and crystalline quality in more detail at beamline P08 at Petra III (DESY) using 25 keV x rays in symmetric Laue geometry. A  $\theta$ - $2\theta$  scan identified the positions of the reflections ranging from (100) to (500) and additional fine rocking scans ( $\theta$  scans) were performed to characterize the individual peaks; see Fig. 4. The setup used a Mythen linear position-sensitive detector (PSD) mounted in vertical scattering geometry. The pixel size in the scattering plane was 50  $\mu\text{m}$  which translates to a  $2\theta$  resolution of 2.7 mdeg. In the direction perpendicular to the scattering plane the detector integrated all intensity with a slit-defined pixel width of 1 mm. The x rays were focused by a set of compound refractive lenses to reach a beam size of about  $100 \times 400 \mu\text{m}^2$  ( $v \times h$ ). The scattered intensity  $I(\theta)$  was determined for every position of  $\theta$  by integrating the signal in the PSD in a range of pixels covering about four times the FWHM. The intensity outside this range

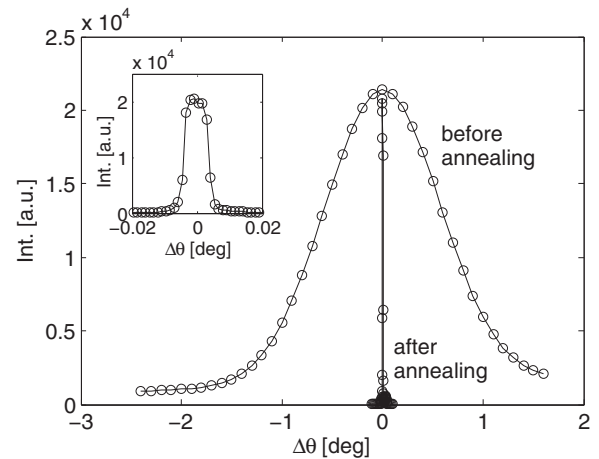


FIG. 3. Rocking curves of the (100) reflection recorded in symmetric Bragg reflection geometry in the initial state of the crystal (as grown), and after the encapsulation process involving annealing. The inset shows a zoom of the narrow rocking curve after annealing. The two data sets were taken at beamline ID10 (ESRF) with 8 keV x rays using different settings, so to facilitate comparison the intensities were scaled to overlap at  $\Delta\theta = 0$ .

was taken as background and subtracted from the signal. The signal was normalized to the intensity after the monochromator to correct for eventual drifts and variations in ring current.

Figure 4 shows  $I(\theta)$  on a logarithmic intensity scale with the five first crystal reflections along the  $(h00)$  direction. There is a marked difference between the intensity of the fundamental reflections,  $h$  even, and the superlattice reflections,  $h$  odd. Both sets get less intense with increasing Miller index  $h$ , due to the decay of the atomic form factor and of the Debye-Waller factor with  $\theta$ .

In the Appendix the intensity data of Fig. 4 are analyzed in terms of dynamical diffraction theory. The results are shown in Fig. 5 as a function of  $Q = |\mathbf{k} - \mathbf{k}'| = \frac{4\pi \sin \theta}{\lambda}$ . The integrated intensities are reasonably well modeled by theory; particularly the ratio between the first three reflections is about right. A scaling factor has been applied to ensure perfect overlap between the model and data at the (200) reflection and in this manner the intensities of the (100) and (300) peaks are also well predicted. The model underestimates the strength of the (400) and (500) reflections. From this investigation it can be concluded that the crystal is indeed nearly perfect. The ratio between fundamental and superlattice reflections indicates that the former are governed by dynamical diffraction while the latter are kinematical due to the weaker structure factor  $F_h \propto (f_{\text{Zn}} - f_{\text{Cu}})$  with only one electron difference between Zn and Cu. The kinematic nature of superlattice peaks will become even more pronounced upon approaching  $T_C$  as the intensity will decrease. Therefore, the experiment we shall describe in the following, elucidating the short- and long-range ordering (SRO and LRO) by monitoring the (100) reflection close to  $T_C$ , must be described in a kinematic framework similarly to the previous neutron scattering experiments, even if the crystal is nearly perfect.

**III. DATA TAKEN IN LAUE SCATTERING GEOMETRY**

We have investigated the temperature dependence of the (100) reflection both below and above  $T_C$  (critical scattering) on two different  $\beta$ -brass crystals and at two different synchrotron beamlines, namely ID10 at ESRF (21 keV) and at P08 at PETRA III (DESY) (25 keV). The results of these experiments are consistent with each other, as will be described below, and also align well with the earlier neutron scattering experiments and the theoretical predictions of the 3d bulk Ising model.

**A. Long-range order**

The integrated intensity variation with temperature as the crystal is rocked through the (100) reflection is shown in Fig. 6. The expected theoretical power law (normalized to fit the amplitude of the data) is shown as the green curve. The correspondence between data and theory is good but the data do not exhibit a sharp truncation at the critical temperature

and an *ad hoc* smearing of the theoretical power law is shown in the zoom on the right panel as the blue curve. We believe that the smearing is related to a lack of precise long-term reproducibility in the relation between temperature and intensity, an effect that we were never able to fully clarify. It manifested itself in a slowly varying (several hours time scale) difference between the actual temperature of the probed crystal volume and the Pt-100 thermometer readout.

Figure 7 shows a typical example of the short-term intensity variation close to  $T_C$ . The scattered intensity was monitored at fixed  $\theta = \theta_B$  while stabilizing the temperature near  $T_C$  and the observed intensity oscillations are almost synchronous with the temperature oscillations in this range within 100 mK from  $T_C$ . The time lag between the thermometer reading and the registered intensity is on the order of one second, or less. On this short time scale the temperature hysteresis, if any, is very small ( $\sim 20$  mK) and indicated by the dashed horizontal lines in Fig. 7. Such behavior is typical of a continuous second-order phase transition as expected here and

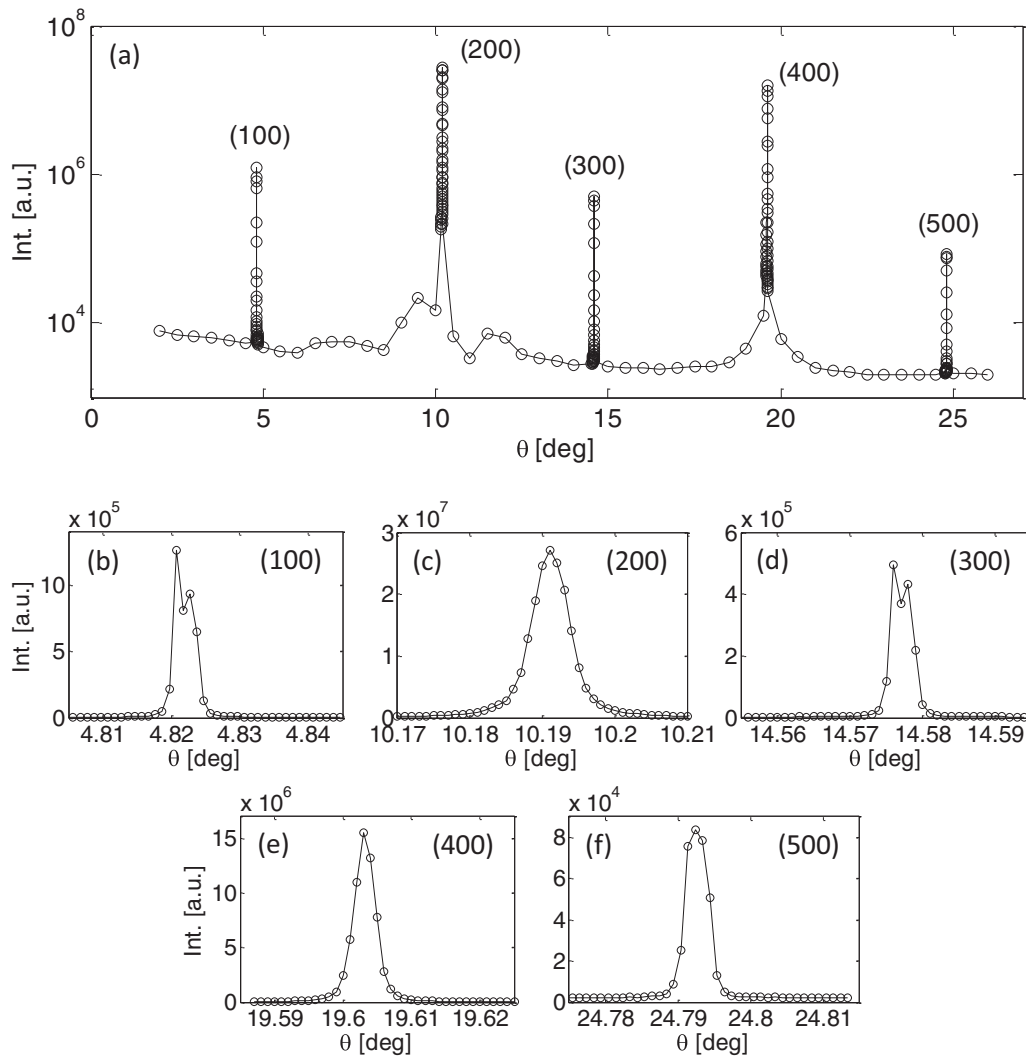


FIG. 4. Two fundamental, (200) and (400), and three superlattice reflections (100), (300), and (500). (a)  $\theta$ - $2\theta$  scan (logarithmic intensity scale) on  $\beta$ -brass in Laue geometry (25 keV) identifying the five reflections. This scan was performed also to verify the absence of  $\gamma$ -phase peaks [6] that otherwise will affect the phase transition. The much finer rocking scans ( $\theta$  scans) on the (100) to (500) positions [(b)–(f)] are superimposed on the figure for comparison. The data were taken at room temperature at beamline P08, Petra III, DESY.

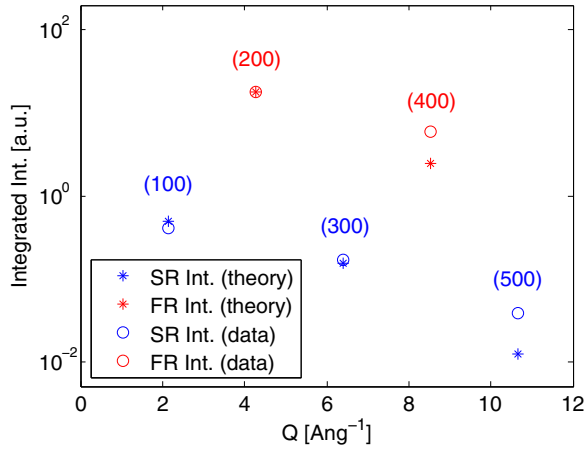


FIG. 5. Comparison between measured integrated intensities of fundamental and superlattice reflections (FR and SR, respectively) and dynamical diffraction theory with the (200) intensity used as normalization; see the Appendix. In a pure kinematic diffraction model the fundamental reflections would be 3 orders of magnitude higher than the superlattice reflections, which is obviously not the case here.

we observed it consistently both in Laue and Bragg scattering geometries.

**B. Short-range order**

Short-range order data were also taken at beamline ID10 (ESRF). A scintillation NaI detector with a front aperture of  $7 \times 7 \text{ mm}^2$  situated 5.5 m behind the sample recorded the scattering. An example is given in Fig. 8 and as expected

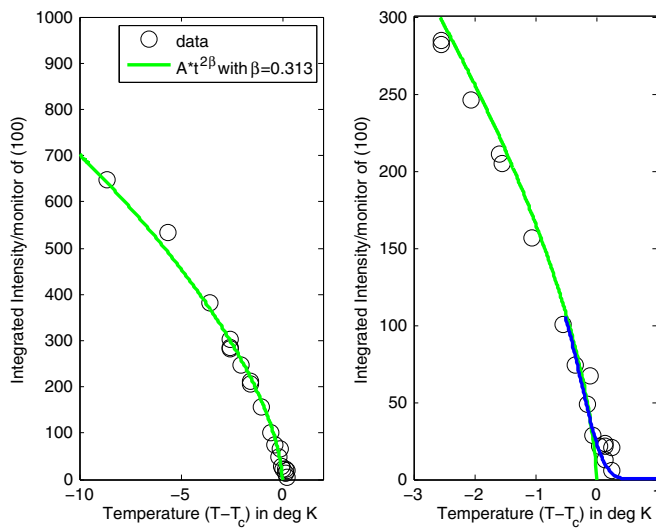


FIG. 6. Left: Power-law behavior of the integrated intensity of the (100) superlattice reflection as  $T_C$  is approached from below (LRO). The Ising model prediction is given by the green curve  $\propto (T_C - T)^{2\beta}$ . Right: Zoom of the near- $T_C$  region illustrating that a Gaussian smearing (standard deviation  $\sigma = 0.2 \text{ K}$ ) of  $T_C$  is required to fit the theoretical prediction (blue line) to the data. Measurements performed at ID10 (ESRF) in symmetric Laue geometry (21 keV x-ray energy).

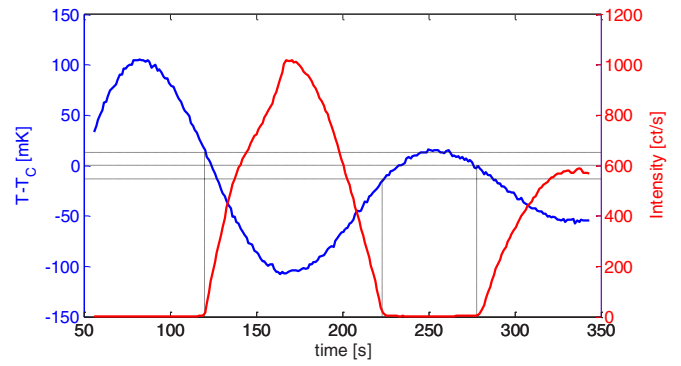


FIG. 7. Temperature and (100) superlattice peak intensity versus time. The intensity vanishes when the temperature is above  $T_C$  and increases (decreases) synchronously with the temperature decrease (increase) when it is below  $T_C$ . The time lag between registered temperature and intensity is less than the integration time (1 s). The data indicate a determination of  $T_C$  to a precision better than  $\pm 0.02 \text{ K}$ , but as explained in the text the precise relation between intensity and temperature exhibited some long-term instability.

for an Ornstein-Zernike correlation function the line shape is Lorentzian with a correlation length  $\xi = \kappa^{-1}$ , where  $\kappa$  is the fitted half-width of peak. The correlation length relative to the nearest-neighbor distance  $a_{nn}$  versus the temperature deviation from  $T_C$  is shown in a double-logarithmic plot in Fig. 9 (black) to illustrate the power-law behavior. The data are consistent with the theoretical prediction of the 3d Ising model shown as the black line both in terms of absolute value and in terms of the critical exponent  $\nu$ . The susceptibility or peak amplitude  $\chi(q = 0)$  is also shown in Fig. 9 (red) and the slope is again in

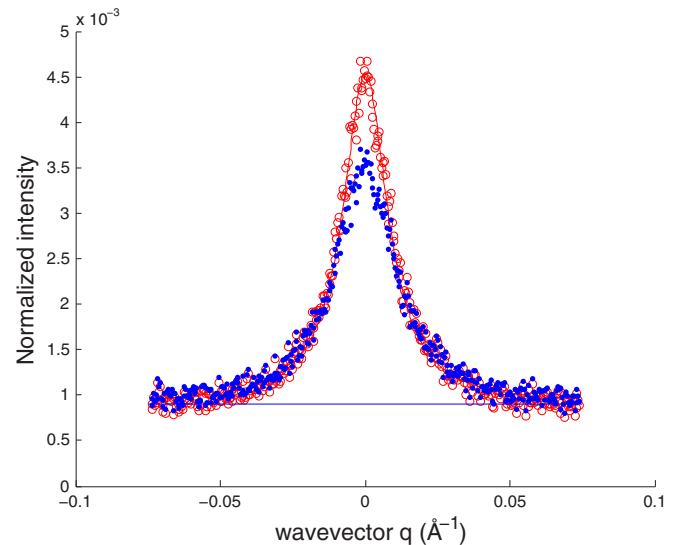


FIG. 8. Critical scattering at a reduced temperature of  $t = 8 \times 10^{-4}$  normalized by the beam monitor intensity. The wave vector  $q$  is determined by the rocking angle  $\delta$  as  $q = G\delta$ . The observed intensity (blue dots) is unfolded with the smearing produced by the finite detector aperture (two-dimensional top-hat function) to yield the red circles. The red full line shows the best Lorentzian fit. The resolution width in the third dimension of reciprocal space is negligible since the wavelength band is very narrow ( $\Delta\lambda/\lambda \sim 10^{-4}$ ).

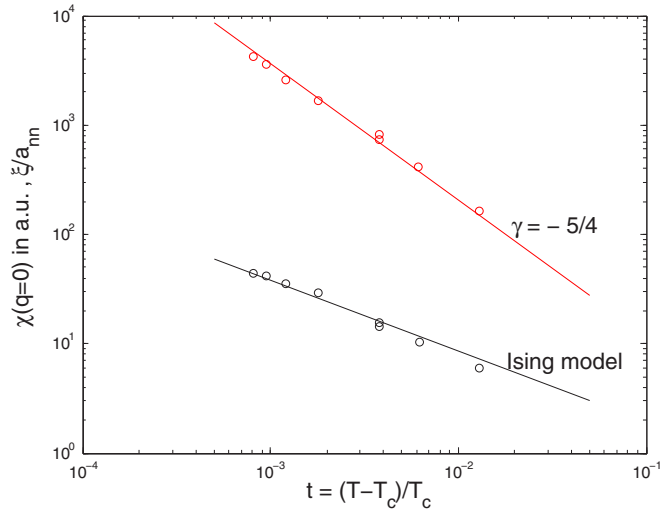


FIG. 9. Correlation range  $\xi$  relative to the nearest-neighbor distance  $a_{nn}$  (black) and susceptibility  $\chi(q=0)$  (arbitrary units) versus reduced temperature  $(T - T_c)/T_c$  (red) obtained from the unfolded line shapes; see Fig. 8. The full black line shows the theoretical prediction of the 3-dimensional Ising model with a slope of  $-\nu$  and  $\nu = 0.64$ . The peak intensity of critical scattering is shown by the red data points yielding a critical exponent  $\gamma = -5/4$ , in accordance with the Ising model.

good accordance with the Ising model when the instrumental resolution is taken into account; see Fig. 8.

We also performed critical scattering experiments in Laue geometry at P08, Petra III (DESY), on a different crystal using 25 keV x rays and the setup with the PSD described in Sec. II. Figure 10 shows examples of critical scattering that again is modeled well with simple Lorentzian profiles. The fitted peak intensity  $\chi(q=0)$  [Fig. 10(a)] is corrected for the resolution function as described above taking the integration limits over the PSD into account. Concerning  $\kappa$ , the peak HWHM, the resolution-induced broadening is so small that it safely can be neglected. Both the susceptibility  $\chi(q=0)$  and the inverse correlation range  $a_{nn}\kappa$  are following the expected power-law behaviors over the entire range in reduced temperature. The data also match the earlier neutron measurements [6] well (red symbols in Fig. 10) and are consistent with data taken at 21 keV at ESRF on a different crystal; see Fig. 9. We conclude that the Laue x-ray data demonstrate the Ising model for critical scattering being valid up to more than 250 nearest-neighbor distances in correlation length [ $4 \times 10^{-3}$  in inverse correlation range; see Fig. 10(b)], i.e., down to a reduced temperature of less than  $10^{-4}$ . This is an important verification step that extends the previous neutron measurements by about two orders of magnitude and was only possible due to the high resolution of synchrotron x ray experiments together with the perfect crystallinity of the  $\beta$ -brass samples.

#### IV. DATA TAKEN IN SYMMETRIC BRAGG REFLECTION GEOMETRY

The results described in this section derive from experiments at beamline P10, PETRA III (DESY), taken at 12 keV x-ray energy with a Pilatus 300k pixel detector (172  $\mu\text{m}$  pixel

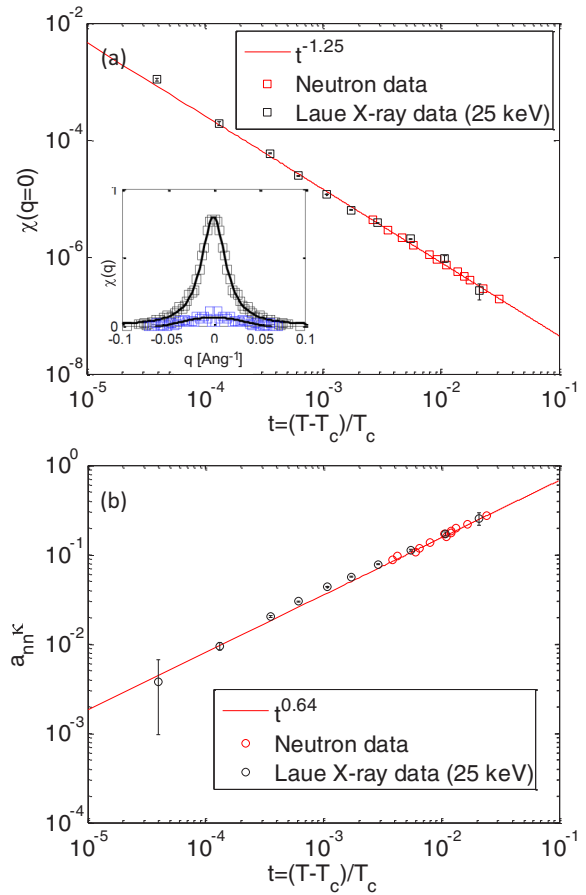


FIG. 10. Critical scattering at the (100) superlattice peak. (a) Fitted amplitude vs reduced temperature  $t$ . Neutron data [6] are shown for comparison together with a power law with critical exponent  $\gamma = -5/4$ . The inset shows two unfolded line shapes (at  $t = 1.1 \times 10^{-3}$  and  $t = 1.1 \times 10^{-2}$ ) and the corresponding Lorentzian fits. (b) Fitted HWHM  $\kappa$  multiplied by the nearest-neighbor distance  $a_{nn}$  to yield the inverse correlation range vs  $t$ . Neutron data are shown for comparison as well as a power law with critical exponent  $\nu = 0.64$ . Data taken in Laue geometry at beamline P08, Petra III (DESY), using 25 keV x rays.

size) 5 m downstream of the sample recording the scattering. The big difference with respect to the transmission Laue data is the near surface sensitivity of the measurement. This occurs due to absorption of the x rays which penetrate only about 0.6  $\mu\text{m}$  into the crystal from the surface. On the contrary, in Laue geometry the entire thickness of the crystal is probed with a uniform sensitivity. To account for the reflection geometry, the furnace inset that holds the sample was modified and the position of the x-ray-transparent windows changed, but apart from that the setup was similar to the Laue case.

At a few occasions we experienced sudden jumps of 0.3–0.5 K in the temperature readout, presumably due to randomly occurring changes in the thermal contact. In addition, there was a slow drift of  $T_c$  over a few days which we attribute to a slow thermal thermalization of the system, but under stable conditions we were able to pass through the phase transition many times without any change in the measured  $T_c$ . This shows that the stoichiometry of the probed volume is constant;

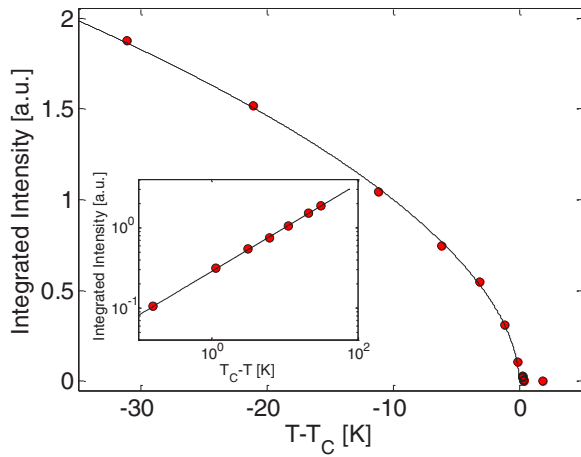


FIG. 11. Integrated intensity of the (100) superlattice peak as a function of temperature taken in symmetric Bragg scattering conditions. The solid line shows the best fit with  $(T_C - T)^{2\beta}$  and yields an exponent of  $\beta = 0.29 \pm 0.01$ . The theoretical prediction for the 3d Ising model is 0.313. The inset shows data on a log-log scale to better visualize the power-law behavior of the integrated intensity.

i.e., similarly to the Laue experiments the sample remained in the pure  $\beta$  phase throughout the experiment. At one occasion the encapsulation was not tight (puncture) which resulted in a rapid drift of  $T_C$  towards smaller values, as expected for dezincification of  $\beta$ -brass, which is therefore easily detectable. The temperature was recorded for every data point in each rocking scan (1–2 min) and the fluctuations were typically 5 mK rms, or better. However, we cannot exclude tiny glitches in the temperature readout from one scan to the following ones.

**A. Long-range order**

The integrated intensity of the (100) superlattice peak was monitored by performing rocking scans ( $\theta$  scans) for every temperature  $T < T_C$  and collecting all the scattered intensities on the detector. The data are shown in Fig. 11. While the best-fitted exponent (0.29) is slightly smaller than the theoretical prediction for the Ising model (0.31) there is no substantial difference between these data taken in Bragg reflection geometry and the data taken in transmission Laue geometry; see Fig. 6. Similarly to the Laue data,  $T_C$  is not perfectly well determined as observed in Fig. 11 where measurements from several temperature series are shown in one plot. The tangent of the data at  $T = T_C$  is not vertical as ideally expected and again this can be modeled as a Gaussian smearing of  $T_C$  with a rms of  $\sim 0.2$  K; cf. the discussion in Sec. III A.

**B. Short-range order**

Concerning the SRO measured in Bragg reflection geometry the situation is different from the Laue case. Due to the small probe volume and the almost identical scattering factors for Cu and Zn the signal is very weak and can only be tracked in a narrow range of temperatures above  $T_C$  before it disappears in the background. SRO data up to 0.48 K above  $T_C$  are

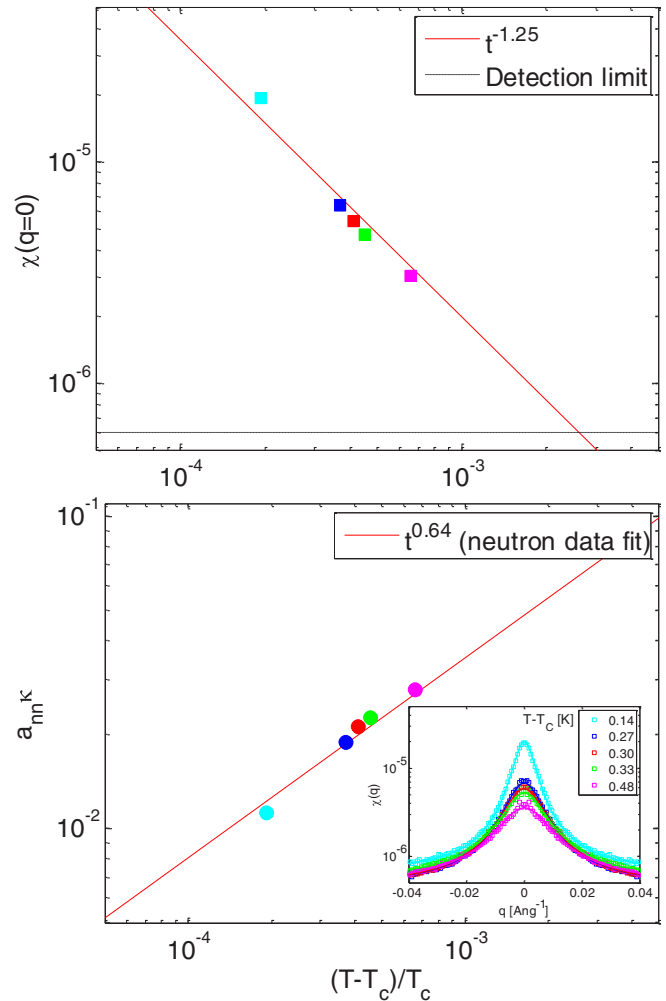


FIG. 12. Amplitude (top) and inverse correlation range (bottom) extracted from the Lorentzian beam profiles (inset) of the SRO. The lines indicate the Ising model and a good correspondence is found. In the bottom plot the red line [identical to that of Fig. 10(b)] is the best fit to the earlier neutron data. The detection limit is derived from the constant background of the line profiles shown in Fig. 13. Data taken at P10, Petra III (DESY), in symmetric Bragg reflection geometry using 12 keV x rays.

shown in Fig. 12. The line profiles are Lorentzian and both the inverse correlation range  $a_{nn}\kappa$  and the susceptibility are in good accordance with the earlier presented x-ray and neutron scattering measurements in Laue geometry. However, due to the limited accessible range a detailed comparison cannot be made. This is significantly different from the Laue data in Fig. 10 where critical scattering could be measured more than 10 K above  $T_C$ .

SRO line profiles have been obtained from Pilatus 2D detector frames assembled in 3d (the third coordinate being  $\Delta\theta$ , the offset from the Bragg angle) and then integrated in spherical shells to yield  $I$  vs  $q$  (Fig. 12, inset). In this case the spatial resolution is much better than the width of the profiles and no resolution-correction terms need to be applied. Close to  $T_C$  the line profiles, shown in Fig. 13, are a superposition of a Lorentzian due to critical scattering and a narrow component which we interpret as LRO Bragg scattering

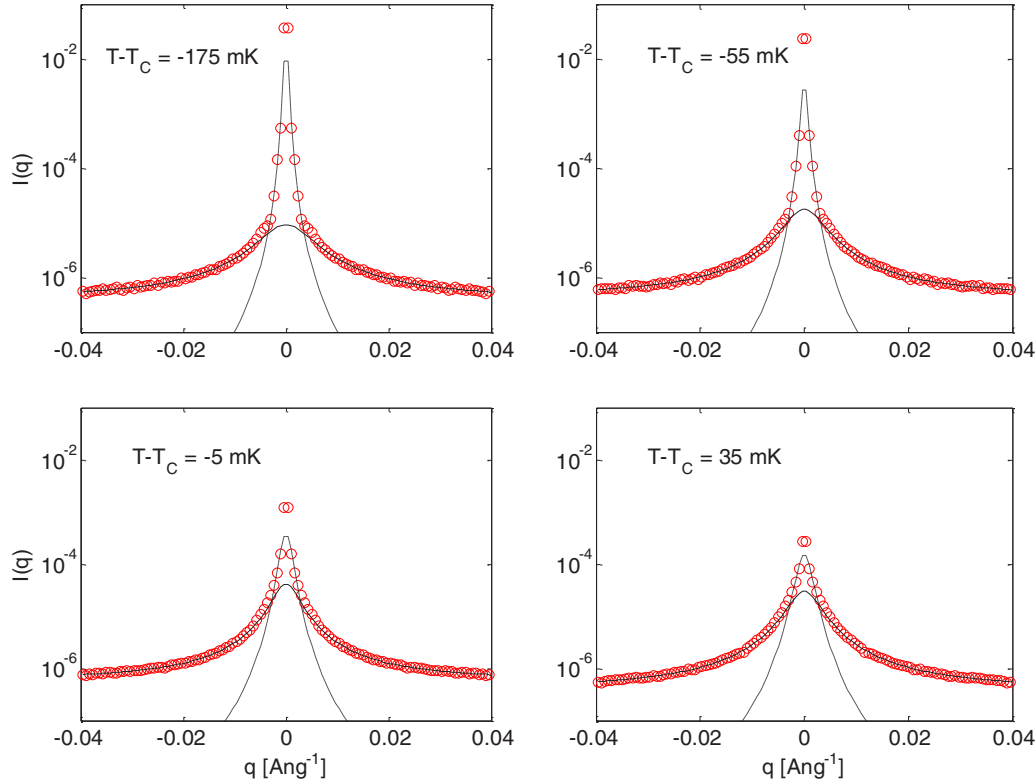


FIG. 13. Integrated line profiles to obtain  $I$  vs  $q$  for different temperature offsets with respect to  $T_C$ . The narrow central component (LRO) is fairly well modeled by a squared Lorentzian, except for the amplitude at  $q = 0$ . The SRO is following a usual Lorentzian line profile similar to the bulk measurements. Data taken at P10, Petra III (DESY), in Bragg reflection geometry using 12 keV x rays.

(SRO-LRO coexistence below  $T_C$ ), although in one case the temperature reading is 35 mK above  $T_C$  (lower right panel). The true temperature could actually be below  $T_C$  because one of the random, tiny, temperature readout glitches may have occurred and we see no good reason to interpret this peak as arising from a second length scale phenomenon. In all cases the narrow component was reasonably well fitted by a squared Lorentzian, except for the amplitude. Similar observations of square Lorentzian peaks have been made in scattering from other critical systems [11,12] where the  $q^{-4}$ -like tails were taken as signs of crystal strain. In our case the squared Lorentzian line shape should be interpreted as a convolution of the experimental resolution function and a possible LRO domain structure. However, we are unable to separate these two contributions and the fitting to a squared Lorentzian serves only the purpose of disentangling the narrow LRO component from the critical scattering which has a single-Lorentzian line shape; see Fig. 13.

The integrated intensity and amplitude of the two components are extracted and shown in Fig. 14 (as hollow circles and stars, respectively) together with the  $\chi(q = 0)$  data for  $T > T_C$  (black dots); see also Fig. 12 (top). The Ising model predictions for LRO and SRO are shown as red and black curves, respectively, and the correspondence with the data is reasonably good, even in the range of coexistence. For the central narrow component the real amplitude (not the square Lorentzian fit amplitude) is used (red stars) to obtain the integrated intensity and the best correspondence with the LRO Ising model. In Fig. 14 the Ising model for LRO (red curve)

has been scaled to match the first red star data point. The open symbols represent the fitted amplitude of the SRO for  $T < T_C$  but the accordance with the Ising model is not as good as

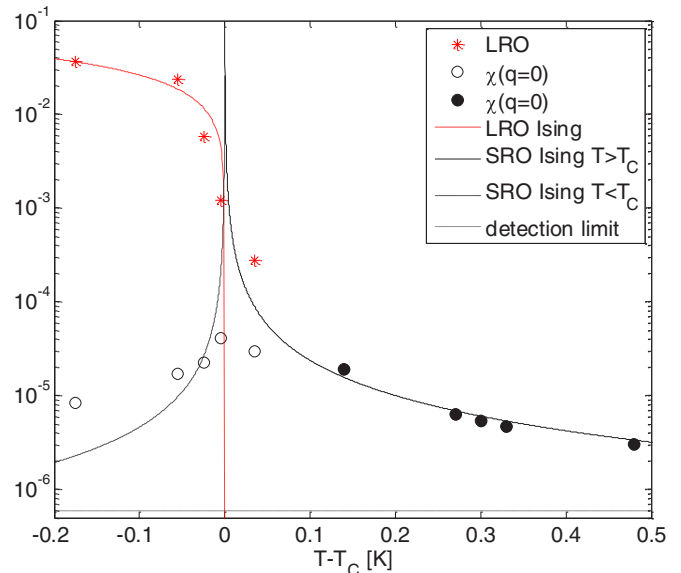


FIG. 14. Summary of the SRO amplitude [ $\chi(Q = 0)$ ] and the integrated intensity of the central component that is assigned with LRO. The lines are Ising model predictions. Data taken at P10, Petra III (DESY), in Bragg reflection geometry using 12 keV x rays.

for the  $T > T_C$  data (black dots). However, the general trend predicted in the coexistence region with an increasing SRO and a decreasing LRO as  $T_C$  is approached from below is evident from the data. Hence, we interpret the central line as LRO Bragg scattering. The central line wings are then caused by diffuse scattering from LRO domain walls where an approximate  $q^{-4}$ -behavior of the intensity indeed is expected (interface scattering).

## V. DISCUSSION AND CONCLUSION

We have studied critical behavior of the temperature-induced order-disorder phase transition in  $\beta$ -brass, nature's archetypical realization of the Ising model for criticality. With our encapsulation technique we were able to perform high-precision measurements of  $\beta$ -brass without the usual problems of dezincification. The short- and long-range order parameters were monitored using x-ray diffraction on the (100) superlattice reflection. A collimated and intense synchrotron beam together with the very small mosaicity of the annealed crystals allowed for superb resolution, so the Ising model predictions could be studied over a wider range of correlation lengths  $\kappa^{-1}$  than ever before (exceeding  $250 a_{nm}$ ), thus providing an important verification step. The Ising model fits the data taken in Laue transmission scattering geometry very well over the full range of temperatures and correlation lengths. In transmission geometry the x rays are essentially a bulk probe, i.e., very similar to the situation in earlier neutron scattering experiments.

We also performed measurements in Bragg reflection geometry where the temperature range in which critical scattering can be measured is strongly reduced. This is caused by the weak scattering contrast between Cu and Zn and because the finite penetration depth ( $< 1 \mu\text{m}$ ) limits the x-ray penetration with only the near-surface region contributing to the scattering. Still, using powerful third-generation synchrotron beams this study is possible. The SRO scattering that can be detected in Bragg geometry fits well with the Ising model predictions, particularly for  $T > T_C$ . In the SRO-LRO coexistence range at  $T < T_C$  the correspondence with theory is less good but given the long-term instability between the temperature reading and the actual sample temperature, it is impossible to conclude any discrepancy between data and theory. The central narrow LRO component does not affect the SRO line shape that remains simple Lorentzian. Hence, within the sensitivity and resolution of the present experiment there is no measurable difference between bulk critical scattering and the result obtained in reflection geometry where only the topmost  $0.6 \mu\text{m}$  of the crystal is probed.

Particularly, we do not find any supporting evidence for two diverging length scales as reported for other critical systems above  $T_C$  and often assigned to surface defects and associated strain [13–21]. Probably, the encapsulation method used here is an advantage and it might also induce less strain than a thin capping layer of metal evaporated onto the crystal, a different method frequently used to keep the stoichiometry intact. Certainly, the excellent crystalline quality we observe after annealing is rarely obtained in other systems and it gives a hint that the sample is close to an ideal realization of the 3d Ising model. Several of the previous observations of two critical

length scales were made in samples displaying structural phase transformations. Indeed, the existence of a thick skin layer where the order parameter is modified by surface effects (defects, strain) appears more credible in such systems than for order-disorder transition materials such as  $\beta$ -brass that may be less vulnerable to structural distortions. However, deeper theoretical considerations or simulations are required to further quantify this statement. We note that in order to make a genuine surface-sensitive measurement (few nm penetration range) a grazing incidence diffraction geometry is required [22,23] but then the signals would become even smaller. In this case, a critical system with greater scattering contrast than  $\beta$ -brass should be chosen to make the experiment feasible [24]. Meanwhile, until surface experiments with ultimate sensitivity eventually have been performed, we conclude that the 3d Ising model with a single diverging length scale holds for the order-disorder transition in  $\beta$ -brass without any restrictions.

A next logical step would be to perform a coherent scattering study of the critical dynamics [25,26] by x-ray photon correlation spectroscopy (XPCS) [27,28]. Due to restrictions in photon energy and sample thickness a coherent scattering experiment is more favorably performed in Bragg than in Laue geometry and indeed we have demonstrated a critical scattering signal under Bragg conditions. However, the count rate in the Pilatus detector amounts to  $\sim 0.3$  photons  $\text{pixel}^{-1} \text{s}^{-1}$  on the peak of the critical scattering shown in Fig. 12 at  $T - T_C = 0.14 \text{ K}$  (cyan data), in this case with an incident beam intensity of about  $5 \times 10^{10}$  photons  $\text{s}^{-1}$ . Such a weak signal will restrict any XPCS investigations to very slow dynamics and it is unlikely that a conclusive test of dynamical scaling [29] can be performed in  $\beta$ -brass given the current limitations in coherent flux.

## ACKNOWLEDGMENTS

Deutsches Elektronen-Synchrotron (DESY) and European Synchrotron Radiation Facility (ESRF) are acknowledged for beam time for this project. The encapsulation was carried out by Rune Christiansen and Flemming Jensen at DANCHIP, Lyngby, Denmark. Initial x-ray investigations were carried out in Poul Norby's laboratory at Risø, DTU, Denmark. We thank F. Zontone, Y. Chushkin, M. Mattenet, C. Deiter, O. Seeck, M. Sprung, A. Ricci, and P. Rinkel for help with the synchrotron experiments. This work has been supported by Carlsbergfondet (The Carlsberg Foundation).

## APPENDIX: DYNAMICAL THEORY FOR LAUE DIFFRACTION

In the following we shall outline the theory for Laue diffraction inspired by Authier [30] and Kato [31]. The polarization  $P$  (dipole moment per volume) of an electron gas with homogeneous density  $\rho$  subject to a homogenous field  $E$  is  $P = -e\rho x$ , where  $x$  is determined from the equation of motion of an electron:  $m \frac{d^2x}{dt^2} = -eE(t)$ . Solving for  $E(t) = E_0 \exp(-i\omega t)$  yields the susceptibility  $\chi$ , defined as  $\chi = \frac{P}{\epsilon_0 E}$ ,

$$\chi = -r_0 \rho \lambda^2 / \pi, \quad (\text{A1})$$

where  $\lambda = 2\pi c/\omega$  is the wavelength and  $r_0 = e^2/(4\pi\epsilon_0 m c^2)$  is the Thomson radius of the electron. For a homogeneous unit

cell in a crystal this can be generalized to

$$\chi_h = \frac{-r_0 \lambda^2 F_h}{\pi V_c}, \quad (\text{A2})$$

where the ratio of structure factor over unit cell volume  $F_h/V_c$  is the effective electron density. In addition to the susceptibility, the Pendellösung length  $\Lambda_0$  is of interest in the Laue case. The Pendellösung effect happens as a result of interference between the diffracted and forward-scattered waves at the exit surface of the crystal. Two waves are excited in each direction with slightly different wave numbers due to refraction. At periodic locations inside the crystal the two forward-scattered waves interfere constructively while at the exact same locations the diffracted waves interfere destructively. At the exit of the crystal this leads to an oscillation of the diffracted intensity vs scattering angle and sample thickness. The period of these oscillations is known as the Pendellösung length and Authier derives it in the symmetric Laue case (assuming a centrosymmetric unit cell and linear polarization) to be [30]

$$\Lambda_0 = \frac{\pi V_c \cos \theta}{r_0 \lambda |F_h|} = \frac{\lambda \cos \theta}{|\chi_h|}. \quad (\text{A3})$$

The corresponding parameter in Bragg reflection geometry is known as the extinction depth given by

$$\Lambda_{\text{ext}} = \frac{V_c \sin \theta}{2r_0 \lambda |F_h|} = \frac{V_c}{4dr_0 |F_h|}, \quad (\text{A4})$$

where  $d = \lambda/(2 \sin \theta) = 2\pi/Q_{hkl}$  is the distance between lattice planes for the given  $(hkl)$  reflection and  $Q_{hkl}$  is the momentum transfer. We measure the integrated intensity  $I_{\text{int}}$  from the  $\beta$ -brass reflections and Kato [31] derives it in the symmetric Laue case to be

$$I_{\text{int}} = A[H(z_0) - 1 + I_0(\xi)],$$

$$H(z_0) = \int_0^{z_0} J_0(z) dz, \quad z_0 = 2\pi t/\Lambda_0, \quad (\text{A5})$$

where  $t$  is the crystal thickness and  $J_0$  and  $I_0$  denote the zeroth-order normal and modified Bessel functions, respectively.  $A$  and  $\xi$  are functions that depend on the susceptibility  $\chi_h$  and the linear absorption coefficient  $\mu$  as

$$A = \frac{\pi |\chi_h|}{2 \sin 2\theta} \exp(-\mu t / \cos \theta), \quad \xi = \frac{\chi_h}{\chi_0} \frac{\mu t}{\cos \theta}. \quad (\text{A6})$$

The integral  $H(z_0)$  of the Bessel function in Eq. (A5) is oscillating around unity but tends to zero for  $z_0 \rightarrow 0$ . This is illustrated in Fig. 15 where the values of  $H$  are indicated for the five studied reflections. For small  $z_0$ , i.e., when  $\Lambda_0$  is large—which happens in the case of weak reflections ( $|F_h|$  small, kinematic limit)—the behavior of  $H$  is almost linear in  $z_0$  and we have  $I_0(\xi) \simeq 1$  so that  $I_{\text{int}}$  is proportional to  $Az_0$ . Thus, we find in the kinematic limit

$$I_{\text{int}} \simeq \frac{r_0^2 \lambda^3 t}{\sin 2\theta \cos \theta} \left( \frac{|F_h|}{V_c} \right)^2 \exp(-\mu t / \cos \theta) \propto |F_h|^2, \quad (\text{A7})$$

which holds for  $z_0 \lesssim 1$ . In the opposite limit for strong reflections and small absorption  $\mu \simeq 0$ , the modified Bessel function is unity,  $H \simeq 1$ , and hence  $I_{\text{int}}$  is approximately equal

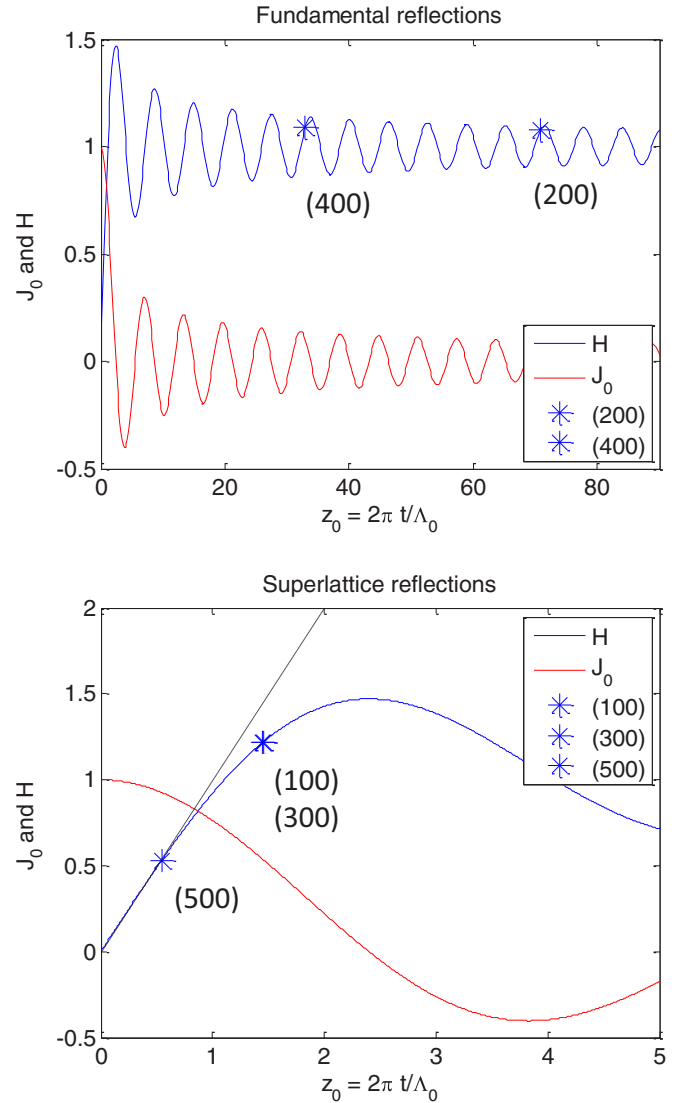


FIG. 15. Illustration of  $J_0(z_0)$  and  $H(z_0)$  for large (top) and small (bottom) values of  $z_0$  according to Eq. (A5). The fundamental reflections (200) and (400) are of dynamic nature due to the high value of  $z_0$  (top). The superlattice reflections have much smaller  $z_0$  and are hence of kinematic nature (bottom). Due to a coincidence, the  $z_0$  values of (100) and (300) are similar, as the structure factor and  $\cos \theta$  almost cancel each other. The solid black line in the bottom plot illustrates the  $z_0 \rightarrow 0$  limit where  $H(z_0) \propto z_0$ .

to  $A$ , i.e.,

$$I_{\text{int}} \simeq \frac{r_0 \lambda^2}{2 \sin 2\theta} \left( \frac{|F_h|}{V_c} \right) \propto |F_h|. \quad (\text{A8})$$

Equations (A7) and (A8) contain the well known result that for dynamic diffraction the integrated intensity is proportional to  $|F_h|$  rather than to  $|F_h|^2$  [32,33].

Equation (A5) can be compared with our experimentally determined integrated intensities. They are simply found by integrating the curves in Figs. 4(b)–4(f) and subtracting a background determined by the signal in the PSD pixels far away from the peak. The result of the comparison is shown in Fig. 5.

- [1] H. E. Stanley, *Introduction to Phase Transitions and Critical Phenomena* (Oxford University Press, Oxford, 1987).
- [2] E. Ising, *Z. Phys.* **31**, 253 (1925).
- [3] M. E. Fisher and R. E. Burford, *Phys. Rev.* **156**, 583 (1967).
- [4] P. Schofield, *Phys. Rev. Lett.* **22**, 606 (1969).
- [5] J. Als-Nielsen and O. W. Dietrich, *Phys. Rev.* **153**, 706 (1967).
- [6] O. W. Dietrich and J. Als-Nielsen, *Phys. Rev.* **153**, 711 (1967).
- [7] J. Als-Nielsen and O. W. Dietrich, *Phys. Rev.* **153**, 717 (1967).
- [8] J. Als-Nielsen, *Phys. Rev.* **185**, 664 (1969).
- [9] R. A. Cowley, *Phys. Scr.* **T66**, 24 (1996).
- [10] D. G. Morris and M. A. Morris, *J. Mater. Sci.* **26**, 1734 (1991).
- [11] D. M. McMorro, N. Hamaya, S. Shimomura, Y. Fujii, S. Kishimoto, and H. Iwasaki, *Solid State Commun.* **76**, 443 (1990).
- [12] S. Ravy, D. Le Bolloch, R. Currat, A. Fluerasu, C. Mocuta, and B. Dkhil, *Phys. Rev. Lett.* **98**, 105501 (2007).
- [13] S. R. Andrews, *J. Phys. C* **19**, 3721 (1986).
- [14] T. W. Ryan, R. J. Nelmes, R. A. Cowley, and A. Gibaud, *Phys. Rev. Lett.* **56**, 2704 (1986).
- [15] K. Hirota, G. Shirane, P. M. Gehring, and C. F. Majkrzak, *Phys. Rev. B* **49**, 11967 (1994).
- [16] T. R. Thurston, G. Helgesen, J. P. Hill, D. Gibbs, B. D. Gaulin, and P. J. Simpson, *Phys. Rev. B* **49**, 15730 (1994).
- [17] M. Altarelli, M. D. Nunez-Regueiro, and M. Papoular, *Phys. Rev. Lett.* **74**, 3840 (1995).
- [18] J. Trenkler, P. C. Chow, P. Wochner, H. Abe, K. E. Bassler, R. Paniago, H. Reichert, D. Scarfe, T. H. Metzger, J. Peisl, J. Bai, and S. C. Moss, *Phys. Rev. Lett.* **81**, 2276 (1998).
- [19] H. Hünnefeld, T. Niemöller, J. R. Schneider, U. Rütt, S. Rodewald, J. Fleig, and G. Shirane, *Phys. Rev. B* **66**, 014113 (2002).
- [20] J. Hlinka, R. Currat, M. de Boissieu, F. Livet, and Y. M. Vysokhanskii, *Phys. Rev. B* **71**, 052102 (2005).
- [21] C. I. Del Genio, K. E. Bassler, A. L. Korzhenevskii, R. I. Barabash, J. Trenkler, G. F. Reiter, and S. C. Moss, *Phys. Rev. B* **81**, 144111 (2010).
- [22] I. K. Robinson, A. A. MacDowell, M. S. Altman, P. J. Estrup, K. Evans-Lutterodt, J. D. Brock, and R. J. Birgeneau, *Phys. Rev. Lett.* **62**, 1294 (1989).
- [23] I. K. Robinson, E. Vlieg, and K. Kern, *Phys. Rev. Lett.* **63**, 2578 (1989).
- [24] F. Livet, F. Bley, J.-P. Simon, R. Caudron, J. Mainville, M. Sutton, and D. Lebolloch, *Phys. Rev. B* **66**, 134108 (2002).
- [25] S. Brauer, G. B. Stephenson, M. Sutton, R. Brüning, E. Dufresne, S. G. J. Mochrie, G. Grübel, J. Als-Nielsen, and D. L. Abernathy, *Phys. Rev. Lett.* **74**, 2010 (1995).
- [26] F. Livet, M. Fevre, G. Beutier, and M. Sutton, *Phys. Rev. B* **92**, 094102 (2015).
- [27] A. Madsen, R. L. Leheny, H. Guo, M. Sprung, and O. Czakkel, *New J. Phys.* **12**, 055001 (2010).
- [28] A. Madsen, A. Fluerasu, and B. Ruta, Structural dynamics of materials probed by x-ray photon correlation spectroscopy, in *Synchrotron Light Sources and Free-Electron Lasers. Accelerator Physics, Instrumentation and Science Applications*, edited by E. Jaeschke, S. Khan, J. R. Schneider, and J. B. Hastings (Springer Verlag, Heidelberg, 2015).
- [29] P. C. Hohenberg and B. I. Halperin, *Rev. Mod. Phys.* **49**, 435 (1977).
- [30] A. Authier, *Dynamical Theory of X-Ray Diffraction* (Oxford University Press, Oxford, 2005).
- [31] N. Kato, *J. Phys. Soc. Jpn.* **10**, 46 (1955).
- [32] J. Als-Nielsen and D. F. McMorro, *Elements of Modern X-Ray Physics*, 2nd ed. (Wiley & Sons, Chichester, 2011).
- [33] T. Matsushita and H. Hashizume, in *Handbook on Synchrotron Radiation*, Vol. 1A, edited by E.-E. Koch (North Holland Publishing Company, Amsterdam, 1983), pp. 261-314.